

Measurement and Modeling of Structure-Induced Surface Scattering on Terahertz Channel

Peian Li, Yapeng Ge, Jiacheng Liu, Wenbo Liu, Jiayuan Cui, Jiabiao Zhao, Qiang Niu, Yuping Yang, Xiangzhu Meng, Yiming Zhao, Jianjun Ma

Abstract—As terahertz (THz) frequencies emerge as promising candidates for next-generation wireless networks, accurate characterization of propagation mechanisms in indoor/outdoor environments becomes essential for system design and performance optimization. This article presents an experimental and theoretical investigation of structure-induced indoor surface scattering on THz channels, examining how material properties and structural configurations jointly govern channel power and angular distribution. Six representative indoor surfaces are characterized, revealing that intrinsic structural inhomogeneity - particularly the quasi-periodic earlywood-latewood arrangement in pine wood - induces measurable angular scattering whose dominant lobes and angular shifts are reproduced by a beam-propagation modeling (BPM) framework. Material-covered surface configurations are further investigated, demonstrating that thin dielectric covering layers can substantially modify reflection characteristics through thickness- and frequency- dependent thin-film interference effects. Wide-angle bistatic measurements conducted in a conference-room environment reveal that structured indoor elements, such as folded curtains, can enhance angular scattering and extend spatial coverage. These findings establish that structure-induced surface scattering mechanisms offer potential for constructing non-line-of-sight THz links in indoor environments.

Index Terms—Indoor channel measurements, material-covered surfaces, structural inhomogeneity, surface scattering, terahertz channel

This work was supported in part by the National Natural Science Foundation of China under Grant 62471033 and in part by the Special Program Project for Original Basic Interdisciplinary Innovation under the Science and Technology Innovation Plan of Beijing Institute of Technology under Grant 2025CX11010. (*Corresponding author: Jianjun Ma.*)

Peian Li, Yapeng Ge, Wenbo Liu, Jiayuan Cui, Jiabiao Zhao, and Xiangzhu Meng are with Beijing Institute of Technology, Beijing 100081, China.

Jiacheng Liu is with Peking University, Beijing 100871, China.

Qiang Niu and Yuping Yang are with Minzu University of China, Beijing 100081, China.

Yiming Zhao and Jianjun Ma are with Beijing Institute of Technology, Beijing 100081, China, and also with the State Key Laboratory of Environment Characteristics and Effects for Near-space, Beijing 100081, China.

I. INTRODUCTION

THE future demand for ultra-high data rates has intensified the exploration of terahertz (THz) frequencies for next-generation wireless networks [1], necessitating accurate characterization and predictive modeling of propagation mechanisms in realistic deployment environments [2, 3]. At THz frequencies, the wavelength becomes comparable to the characteristic dimensions of surface features and material inhomogeneities commonly encountered in indoor settings [4, 5], rendering THz channels highly sensitive to surface textures, dielectric properties, and geometric configurations - giving rise to intricate reflection and scattering phenomena that fundamentally govern channel characteristics [6]. Indoor THz channel propagation is predominantly determined by its interactions with environmental surfaces, particularly for non-line-of-sight (NLoS) transmission paths when direct propagation is obstructed. Reconfigurable intelligent surfaces (RIS) and metasurface-based structures have been proposed to actively control channel propagation through phase and amplitude manipulation [7, 8], demonstrating beam steering and coverage enhancement capabilities [9, 10]. However, such engineered reflective structures typically entail increased system complexity, elevated fabrication costs [11], and limited robustness to environmental variations.

An alternative research direction focuses on understanding and exploiting material-dependent channel propagation inherent to the THz band [12]. Experimental and theoretical investigations have demonstrated that material composition and surface characteristics, particularly roughness, can significantly alter channel scattering patterns and power redistribution [13, 14]. Measurement-based studies have further quantified the reflection, transmission, and scattering coefficients of common building materials, providing essential empirical inputs for THz channel modeling [5, 15]. In parallel, scattering-aware modeling frameworks have been developed to capture the frequency- and angle- dependent interactions between THz channels and material surfaces, thereby enhancing propagation prediction accuracy in complex environments [16, 17]. From this perspective, leveraging the intrinsic reflection and scattering properties of existing environmental surfaces - such as walls, ceilings, and other architectural elements - offers a low-complexity,

TABLE I
MEASUREMENT AND MODELING OF COMMON BUILDING MATERIALS

Frequency	Method	Sample	Contributions	Ref.
97.05 GHz	Continuous wave	Basswood sheets, gypsum sheets, cement mortar sheets	Water content detection, defect detection	[26]
113-170 GHz		Glass door	Transmission loss, reflectivity	[18]
0.2-3 THz	Terahertz time-domain spectroscopy	Ceramic, gypsum plasterboard, polymethyl methacrylate, soda-lime float glass	Dielectric parameters, attenuation coefficient, refractive index, electrical conductivity	[19]
200-500 GHz		Glass, concrete, granite	Complex permittivity, reflectance, transmittance	[20]
300 GHz		Bricks, stone, cement, gypsum, wood	Scattering coefficients, refractive indices	[5]
0.2-1.2 THz		Corroded steel plates	Attenuation, absorption coefficient, refractive index, corrosion thickness	[27]
100-400 GHz	Terahertz frequency-domain spectroscopy	Glass, ceiling board	Transmission coefficient, dielectric permittivity	[28]
219-224 GHz	Vector network analyzer	Glass, granite, polyvinyl chloride board, ceramic, wooden board	Transmission and reflection coefficients, complex permittivity	[15]
140-210 GHz		Plexiglass, nylon	Complex permittivity	[21]
282-290 GHz		Glass, polyvinyl chloride board, marble, plaster, raw wood	Complex permittivity, reflection and transmission coefficients	[29]

deployment-friendly approach for constructing robust NLoS THz links without requiring dedicated engineered reflectors [13, 18].

Common indoor construction materials, including drywall, wallpaper, plywood, and PVC panels, exhibit diverse electromagnetic responses arising from variations in microstructure, dielectric properties, and surface roughness, which can significantly influence channel degradation, angular scattering distributions, and multipath characteristics [19-21]. Accurate measurement and modeling of material electromagnetic parameters and reflection characteristics across the terahertz spectrum are therefore widely regarded as essential prerequisites for realistic channel modeling and system performance evaluation. To support such efforts, various measurement techniques operating in either the time domain or the frequency domain have been employed to characterize key electromagnetic parameters relevant to THz channel propagation, with representative studies summarized in Table I. Building upon these, empirical reflection and scattering data have been integrated into ray-tracing frameworks and statistical channel models [22, 23], enabling more accurate reconstruction of multipath performance and spatial power distribution in both indoor and urban scenarios. Despite these advances, existing studies predominantly focus on simplified or homogeneous surface conditions [24, 25], neglecting structured or inhomogeneous boundary conditions that occur naturally indoors. In this work, we target three practically common structure classes - internal quasi-periodic inhomogeneity (pine growth layers), smooth/rough metallic substrates covered by thin lossy dielectrics (thin-film interference), and room-scale folded fabric elements (curtain-induced angular spreading) - and we provide measurement-validated, physics-based models tailored to each class.

The remainder of this article is organized as follows: Section II presents material characterization and investigates

structure-induced scattering arising from intrinsic material inhomogeneity. Section III examines scattering behaviors of material-covered surfaces, highlighting the role of surface-level composite structures. Section IV reports wide-angle indoor measurements that reveal environment-induced scattering effects originating from structured indoor elements in realistic propagation scenarios. Finally, Section V concludes the article with a summary of key findings.

II. CHARACTERIZATION OF SINGLE-MATERIAL SURFACES

A. Samples Preparation and Characterization

Realistic indoor environments typically comprise a substantially broader variety of materials, including decorative surface coatings and soft furnishings [30], whose electromagnetic and structural characteristics can differ markedly from those of conventional rigid surfaces. To extend the investigation of material-dependent THz channel propagation to more representative indoor scenarios, six commonly encountered materials - wall plaster, leather, PVC leather, wallpaper, pine wood, and curtain - were selected in this work. As illustrated in Fig. 1(a), these materials exhibit varying surface textures and can be considered electromagnetically smooth at low-THz frequencies [31], since their surface roughness remains substantially smaller than the operating wavelength according to the Rayleigh roughness criterion [4].

The tested samples were collected from realistic indoor environments and common furnishings, with thicknesses exhibiting inherent variability. For each sample, thickness was measured at multiple points within the illuminated region, and these uncertainties were propagated into the extracted complex permittivity. Among these materials, the pine wood sample is of particular interest due to its intrinsic structural inhomogeneity arising from the alternating arrangement of earlywood (low-density) and latewood (high-density) regions,

as illustrated in Fig. 1(b). This periodic density variation, characterized by effective period (G) along the orientation direction (s), is a well-documented feature of softwood species known to influence electromagnetic wave interactions at THz frequencies [32, 33]. Despite these structural and thickness variations, accurate electromagnetic parameters were extracted using the well-known amplitude transmission function of a parallel dielectric slab [34], with the influence of such variations explicitly considered in the subsequent analysis.

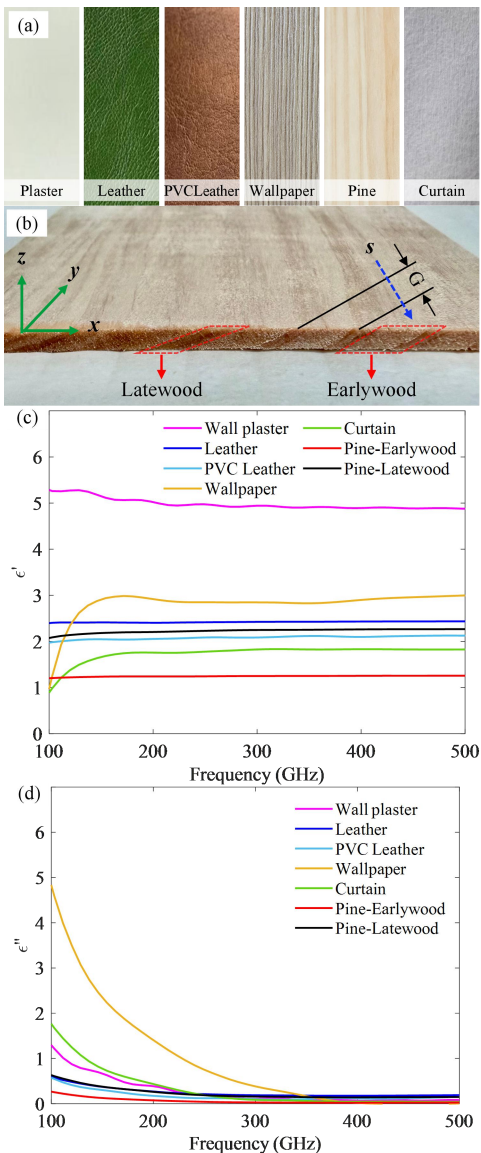


Fig. 1. (a) Surface morphology of the materials under test. (b) Cross-sectional view of the pine wood sample, where G denotes the period of the alternating earlywood-latewood structure, s indicates the orientation of the periodicity, and x , y , and z represent the geometric axes of the wood sample. (c) Measured real part of the dielectric permittivity of the tested materials as a function of frequency. (d) Measured imaginary part of the dielectric permittivity of the tested materials as a function of frequency. (Thickness of wall plaster: 1.21 mm; leather: 2.22 mm; PVC leather: 1.66 mm; wallpaper: 0.22 mm; pine wood: 2.73 mm for earlywood specimen, 2.03 mm for latewood specimen; and curtain: 0.35 mm).

Fig. 1(c) and Fig. 1(d) present the measured real (ϵ') and imaginary (ϵ'') parts of the complex dielectric permittivity as a function of frequency measured by a T-SPEC 800 THz-TDS

system, revealing pronounced variations among materials [35, 36]. Wall plaster exhibits the highest real permittivity ($\epsilon' \approx 5$), consistent with its mineral-based composition, whereas curtain fabric and wallpaper display lower values ($\epsilon' \approx 1.5$ -2.0) due to their porous microstructures. Materials sharing similar base constituents, such as PVC wallpaper and PVC leather, exhibit discernible differences attributable to variations in fabrication processes and filler distributions. Of particular significance is the substantial contrast between earlywood and latewood specimens. The latewood region exhibits consistently higher ϵ' and ϵ'' values due to its greater cell wall density and reduced porosity [37], consistent with effective medium theory predictions [32, 38]. This density-dependent permittivity variation within a single material gives rise to spatially varying electromagnetic properties, inducing structure-dependent scattering phenomena that will be examined in the following subsection.

B. Experimental Measurement

A continuous-wave (CW) measurement system operating in the D-band was employed, as illustrated in Fig. 2(a). At the transmitter (Tx) side, a signal generator (Ceyear 1465D) produced a stable RF signal with an output power of 0 dBm, which was subsequently up-converted to the 113-170 GHz frequency range using a $\times 12$ frequency multiplier (Ceyear 82406B). The resulting terahertz signal was radiated through a standard horn antenna (HD-1400SGAH25) coupled with a polytetrafluoroethylene (PTFE) dielectric lens having a focal length of 10 cm, yielding a combined antenna gain of approximately 25 dBi at 140 GHz. An identical horn was employed at the receiver (Rx) side, and the received power was recorded using a calibrated power sensor (Ceyear 71718). Measurements were conducted at three representative frequencies - 113, 140, and 170 GHz - spanning the D-band to capture frequency-dependent propagation characteristics. The channel beam was directed onto the surface of the material under test (MUT) at a controlled incident angle, with the sample mounted vertically with respect to the optical table. To characterize the angular scattering behavior induced by material interactions, the receiver was mounted on a computer-controlled rotating platform and scanned in 1° increments to record the angular distribution of received power arising from material-induced reflection and scattering. The distances from the MUT to both the transmitter and the receiver were fixed at 34 cm, resulting in a total propagation path length of 68 cm for all measurement configurations. To ensure measurement integrity and minimize parasitic reflections, the MUT was carefully positioned with respect to surrounding metallic structures, including the aluminum profiles comprising the experimental support frame.

For reflection measurements, a polished aluminum plate served as a reference for total-reflection response [4]. As shown in Fig. 2(a), the incident channel impinged on the material surface at 45° , with reflected and scattered signals captured by the rotating receiver. Here, only results at 140 GHz are presented, as observations at 113 GHz and 170 GHz exhibited consistent trends. Fig. 2(b) shows that all tested

materials exhibit a dominant specular reflection component centered at the geometric reflection angle (law of reflection). Wall plaster exhibits the strongest reflection while curtain fabric shows the weakest, consistent with the permittivity trend in Fig. 1(c). Note that the reflection results in Fig. 2(b) (shown by the red curve) were obtained from a large pine wood plate featuring alternating earlywood and latewood structures (see Fig. 1(b)), thus representing an effective average over the spatially inhomogeneous internal structure [39]. For transmission measurements, a line-of-sight (LoS) configuration was established with normal incidence on the material surface, and the receiver was rotated to scan angular directions on both sides of the direct transmission path (0°). Free-space transmission served as the reference baseline. As shown in Fig. 2(c), although material thickness variations introduce differences in absolute transmitted power, the overall angular transmission characteristics remain largely preserved across samples. Notably, the pine wood sample exhibits pronounced fluctuations and cannot be explained by bulk dielectric properties (single-layer homogeneous dielectric slab) alone, suggesting the influence of internal structural inhomogeneity from the periodic earlywood-latewood arrangement. The underlying physical mechanism is analyzed through dedicated modeling later.

C. Structure-induced Scattering

Pine wood exhibits quasi-periodic internal inhomogeneity from alternating earlywood ($\sim 0.29 \text{ g/cm}^3$) and latewood ($\sim 0.64 \text{ g/cm}^3$) layers [32, 38] resulting in corresponding variations in electromagnetic properties at THz frequencies, as shown in Fig. 1(c)-(d). When cut perpendicular to the growth-ring direction, this internal structure can be regarded as a laterally modulated dielectric medium. As illustrated in Fig. 1(b), the effective spacing between adjacent growth layers is approximately $G = 15 \text{ mm}$ with a duty cycle (defined as the fractional width of the latewood layer within one effective period) of $D = 0.25$, and the modulation direction s forms an angle of $\psi = 25^\circ$ with respect to the z -axis. Given the sample geometry ($L \times W \times H$: $150 \times 100 \times 3 \text{ mm}^3$) and the effective channel beam diameter of approximately 24 mm , the growth layers within the illuminated region can be reasonably approximated as quasi-parallel stratified structures with uniform inclination, allowing the ring curvature to be neglected in subsequent analysis.

To establish a quantitative connection between the experimentally observed angular scattering characteristics and the internal growth-layer structure of pine, the refractive-index inhomogeneity is approximated as a locally periodic tilted modulation over the illuminated aperture, providing a tractable idealization of the quasi-periodic growth-layer morphology. Accordingly, a local coordinate along the growth-layer direction is introduced as

$$s(x, z) = x \sin \psi + z \cos \psi \quad (1)$$

where the modulation direction s and the coordinate system (x, y, z) follow the geometric definitions shown in Fig. 1(b), and the modulation is assumed to be invariant along the y -direction.

Such a structure can be naturally incorporated into a beam-propagation model (BPM) [40] inspired by diffraction theory. The propagation of the complex electric field $E(x, y, z)$ inside the pine sample is governed by the scalar Helmholtz equation [40, 41], as

$$\nabla^2 E + k_0^2 n^2(x, y, z) E = 0 \quad (2)$$

where k_0 denotes the free-space wavenumber and $n(x, y, z)$ represents the spatially varying refractive index distribution. To enable efficient numerical propagation, the refractive-index distribution is decomposed into a spatially averaged background component and a position-dependent perturbation

$$n(x, y, z) = n_0 + \delta n(x, y, z) \quad (3)$$

where n_0 represents the averaged refractive index of pine, and $\delta n(x, y, z)$ denotes the refractive-index perturbation

$$\delta n(x, y, z) = \begin{cases} \delta n_H, \text{mod}(s, G) < DG \\ \delta n_L, \text{otherwise} \end{cases} \quad (4)$$

with δn_H and δn_L corresponding to the refractive-index deviations of the latewood and earlywood layers, which can be extracted from THz-TDS measurements.

The propagation through the sample thickness d is discretized into N steps with step size $\Delta z = d/N$. Substituting (3) into (2) and invoking the paraxial approximation, the field evolution is approximated using a split-step beam-propagation scheme, in which transverse diffraction in a homogeneous background medium and the local complex material response are treated sequentially within each propagation step. Following standard beam-propagation and angular-spectrum formulations [42, 43], the diffraction contribution is evaluated in the spatial-frequency domain, yielding the angular-spectrum propagation operator,

$$H(k_x, k_y) = \exp\left(-i \frac{k_x^2 + k_y^2}{2k_0 n_0} \Delta z\right) \quad (5)$$

where k_x and k_y denote the transverse spatial-frequency components. This operator is derived from the angular-spectrum representation of the scalar Helmholtz equation under the paraxial condition $k_x^2 + k_y^2 \ll (k_0 n_0)^2$, which is satisfied here because the measured/simulated power concentrates within the central lobe and first-order lobes, and the residual power beyond this range is close to the measurement noise floor.

Let the complex refractive index be $n^*(x, y, z) = n(x, y, z) - i\kappa(x, y, z)$, with n the phase index and κ the extinction coefficient. We decompose $n(x, y, z) = n_0 + \delta n(x, y, z)$, $\kappa(x, y, z) = \kappa_0 + \delta \kappa(x, y, z)$. The per-step material operator is then

$$M(x, y, z) = \exp(ik_0 \delta n(x, y, z) \Delta z) \exp(-k_0 \delta \kappa(x, y, z) \Delta z) \quad (6)$$

while the background phase/attenuation due to n_0 , κ_0 is included in the homogeneous propagation term.

After propagating to the exit interface $z = d$, we treat the angular pattern comparison as relative and therefore omit absolute scaling constants. Because the transmission measurement is performed at (near-) normal incidence, we neglect refraction-induced remapping of transverse spatial frequencies at the exit interface and map propagating components via $k_x = k_0 \sin \theta_s$ in air. The FFT grid and sampling

are chosen such that the far-field angular resolution matches the 1° receiver scan.

Within this modeling framework, the role of key structural parameters in shaping the angular scattering response can be systematically assessed. Variations in the effective period G constitute one of the key factors governing the angular position of the first side-lobe, as illustrated in Fig. 3(a). By comparing the calculated scattering distributions corresponding to $G = 13, 15,$ and 17 mm, an angular shift of approximately 1.8° is observed for the principal off-axis lobe, while the overall envelope of the angular distribution remains largely unchanged. To further examine the influence of realistic structural variations on scattering behavior, the pine plate (see Fig. 1(b)) was translated along the x -direction by ± 5 mm and ± 10 mm, leading to an effective period G within the illuminated region that varies approximately between 13 and 17 mm, respectively. The measured scattering distributions

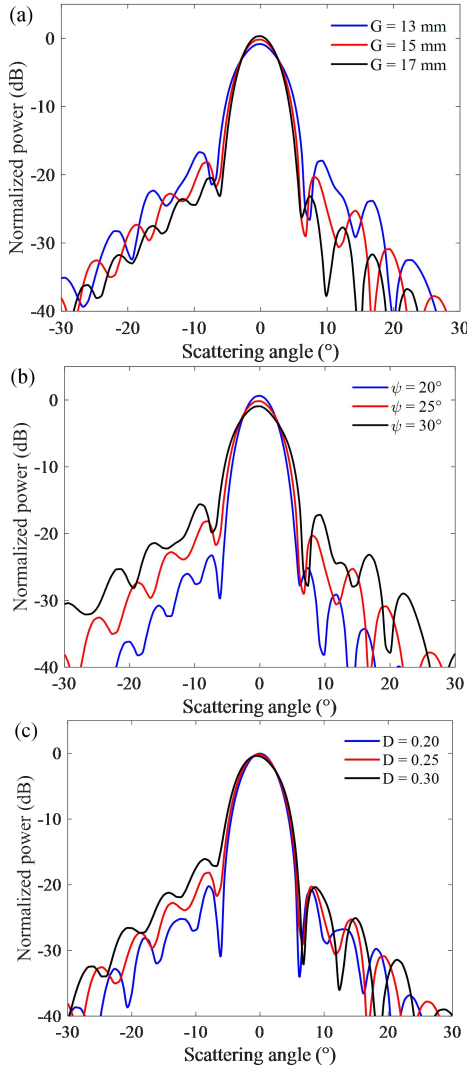


Fig. 3. (a) Calculated angular scattering distributions for different effective periods G , where G represents the spacing between adjacent growth layers. (b) Calculated angular scattering distributions for different tilt angles ψ , where ψ represents the angle between the modulation direction s and the z -axis. (c) Calculated angular scattering distributions for different duty cycles D , where D represents the fraction of the latewood layer within one effective period.

shown in Fig. S1 of the Supplementary Information indicate that the angular position of the first side-lobe is close to the predicted value. As the illuminated position varies, a corresponding shift in the angular position of the first side-lobe is observed, with an angular variation of approximately 2° , which is close to the predicted range shown in Fig. 3(a). Similarly, the structural tilt angle ψ is also found to exert a noticeable influence on the angular scattering characteristics, as illustrated in Fig. 3(b). As ψ increases, the side-lobes gradually shift further away and become more pronounced. This behavior reflects the role of ψ in modifying the effective transverse projection of the internal periodic structure, as defined in (1), which governs the transverse coupling efficiency and consequently shapes the angular redistribution of scattered energy [40].

In contrast to G and ψ , variations in the duty cycle D exert a relatively minor influence on the angular position of the first side-lobe and the overall scattering envelope, while primarily inducing a small angular shift of the main lobe (on-axis) of about 0.6° , as illustrated in Fig. 3(c). This behavior indicates that the duty cycle governs the amplitude of the internal refractive-index modulation, thereby regulating the transverse coupling efficiency into different angular scattering channels without introducing additional angular components [44].

It should be noted that density variations associated with natural growth processes, as well as the relative orientation between the artificial cutting direction and the annual-ring structure, may influence the effective period G , the tilt angle ψ , and duty cycle D , thereby inducing variations in the resulting scattering behavior. These variations arise from the combined effects of multiple structural factors.

III. CHARACTERIZATION OF COVERED SURFACES

Building upon the structure-oriented scattering mechanisms identified for single-material interfaces in Section II, this section extends the analysis to composite boundary conditions formed when a substrate is covered by an additional material layer. Such material-covered surfaces are ubiquitous in practical indoor environments, commonly encountered when metallic frames, cabinets, appliances, and structural elements are partially or fully coated by wallpapers, fabrics, decorative laminates, or other functional coverings.

A. Scattering by Covered Smooth Surfaces

We consider a practically relevant configuration consisting of a smooth metallic reflector covered by a homogeneous dielectric material layer. This scenario commonly arises in indoor environments when metallic panels, frames, or appliances are partially or fully covered by decorative or functional materials. By employing a polished aluminum plate as the reference substrate, geometric irregularities and surface-roughness-induced distortions are minimized, thereby allowing the analysis to focus specifically on the electromagnetic effects introduced by the material covering layer on the reflected power and angular response.

Under the same reflection geometry described in Section II-B and illustrated in Fig. 2(a), angular scattering

distributions were measured for a bare aluminum plate and for the same plate covered with representative indoor materials, namely wallpaper and leather. The aluminum plate has dimensions of 100 mm × 100 mm × 5 mm. Each covering layer was cut to identical dimensions and attached along the edges to ensure near-conformal contact with the metallic substrate, thereby minimizing residual air gaps between the covering layer and the metal surface.

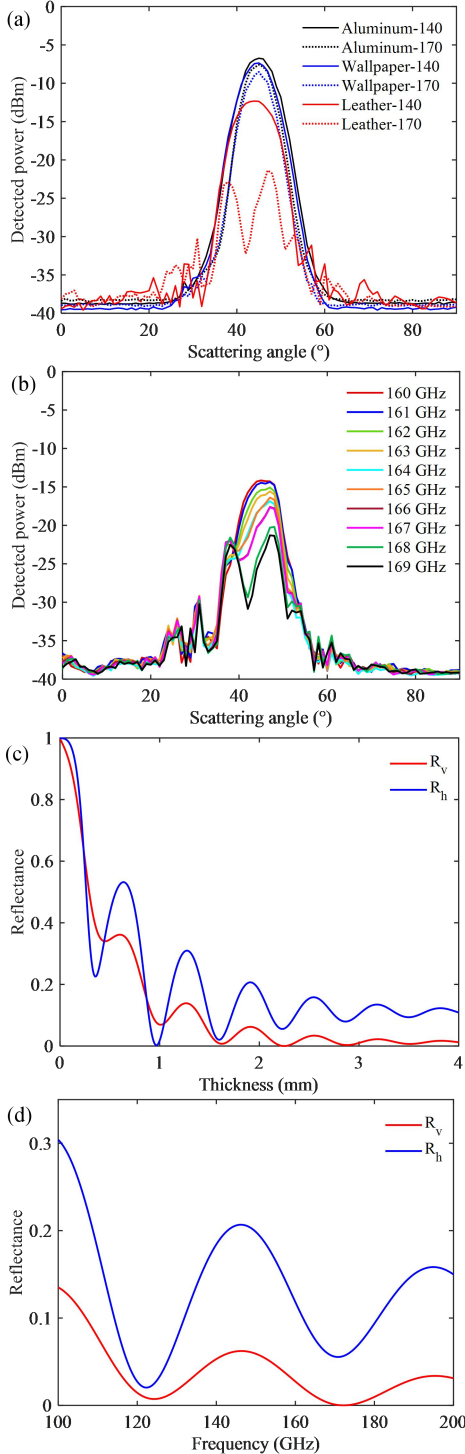


Fig. 4. (a) Scattering distributions of material-covered surface. (b) Frequency-dependent scattering distributions of an aluminum plate covered by leather. (c) Calculated reflectance at 170 GHz as a function of the covering material thickness. (d) Calculated reflectance as a function of frequency for a fixed covering thickness.

Angular scattering distributions were measured at 113, 140, and 170 GHz. For clarity, Fig. 4(a) presents representative results at 140 and 170 GHz, highlighting the contrast between typical scattering behavior and the frequency-dependent deviations observed at higher frequencies. The material-covered surfaces exhibit a reduction in detected power around the specular direction compared to the bare aluminum reference, attributable to additional power loss and impedance mismatch introduced by the covering layer. For the wallpaper-covered configuration, the overall angular profile remains similar to that of the bare aluminum plate, suggesting that the response continues to be dominated by specular reflection from the underlying metal surface, with the thin wallpaper layer contributing primarily to additional insertion loss rather than altering the angular shape of the specular lobe. [45].

In contrast, the leather-covered configuration at 170 GHz exhibits a pronounced suppression and deformation of the angular response near the specular direction, deviating substantially from the expected single-peaked profile. To investigate whether this anomalous behavior exhibits frequency dependence, additional angular scattering measurements were conducted for the leather-covered surface from 160 to 169 GHz in 1 GHz increments, as shown in Fig. 4(b). As the frequency decreases from 169 GHz toward 160 GHz, the distorted profile gradually evolves into a well-defined single-peaked specular response, accompanied by a progressive recovery of the specular reflection component. This trend confirms that the distortion observed at 170 GHz is strongly frequency dependent. Given that the leather layer (thickness 2.22 mm) is substantially thicker than the other covering materials examined, the observed behavior is hypothesized to be associated with the effective optical thickness of the covering layer. Specifically, coherent multiple reflections within the dielectric layer can substantially modify the effective reflectance at the metal interface through thin-film interference effects [46].

To quantitatively examine this hypothesis, the material-covered metallic surface is modeled as a planar three-layer structure consisting of air (medium 1), a lossy dielectric covering layer (medium 2), and a metallic substrate (medium 3). The analysis focuses on the coherent specular reflection component and adopts a transfer-matrix thin-film formulation in which multiple internal reflections and material absorption are explicitly incorporated. For an obliquely incident plane wave at angle θ_i with respect to the surface normal, refraction inside the dielectric layer is governed by Snell's law generalized to complex permittivity. Assuming non-magnetic media ($\mu_r \approx 1$) [47, 48], the complex refraction angle inside the covering layer can be expressed [9, 49] as

$$\theta_2 = \arcsin\left(\frac{\sqrt{\varepsilon_1}}{\sqrt{\varepsilon_2}} \sin \theta_i\right) \quad (7)$$

where ε_1 , ε_2 , ε_3 denote the complex permittivities of air, the covering material, and the metallic substrate, respectively. The Fresnel reflection coefficients at the air-cover interface ($\rho_{h/v}^{12}$)

and the cover-metal interface ($\rho_{h/v}^{23}$) are computed for both horizontal (h) and vertical (v) polarizations using the standard Fresnel equations. The coherent round-trip propagation inside the covering layer of thickness d is described by the complex phase factor [50]

$$P(d, f) = \exp(-2\alpha d \cos \theta_2) \exp(-j2\beta d \cos \theta_2) \quad (8)$$

where f is the operating frequency. The phase constant β and attenuation constant α inside the lossy dielectric layer are implicitly contained within the complex propagation constant $k_2 = k_0 \sqrt{\epsilon_2} = \beta - j\alpha$. The longitudinal propagation constant inside the covering layer is given by $k_{z,2} = k_2 \cos \theta_2$. Since the covering material exhibits non-negligible loss, ϵ_2 is complex-valued as determined by the THz-TDS measurements presented in Section II-A, and (8) inherently accounts for both phase accumulation and absorption-induced amplitude decay during coherent round-trip propagation within the layer.

The coherent specular reflection from the material-covered metallic interface is modeled using the Fresnel-Airy formulation for a lossy dielectric slab. The effective complex reflection coefficient is obtained by summing the multiple internal reflections within the covering layer, as

$$\rho_{h/v}(d, f) = \frac{\rho_{h/v}^{12} + \rho_{h/v}^{23} P(d, f)}{1 + \rho_{h/v}^{12} \rho_{h/v}^{23} P(d, f)} \quad (9)$$

and the corresponding specular reflectance is given by

$$R_{h/v}(d, f) = |\rho_{h/v}(d, f)|^2 \quad (10)$$

Based on the above thin-film interference model, Fig. 4(c) presents the calculated reflectance at 170 GHz as a function of covering layer thickness for both horizontal (R_h) and vertical (R_v) polarizations, using the complex permittivity values extracted from THz-TDS measurements. As the thickness varies, pronounced oscillations in both R_h and R_v are observed, arising from the combined effects of coherent phase interference and material absorption within the covering layer [51]. Notably, for a leather thickness of 2.22 mm corresponding to the actual sample, the calculated reflectance reaches a local minimum for both polarizations, in excellent agreement with the experimentally observed power suppression at 170 GHz shown in Fig. 4(a).

Fig. 4(d) further presents the calculated reflectance as a function of frequency for the fixed leather covering thickness of 2.22 mm. As the frequency increases from 100 GHz toward 170 GHz, the reflectance decreases progressively and reaches a minimum near 170 GHz, while remaining significantly higher at frequencies around 140 GHz. This frequency-dependent trend closely reproduces the evolution observed in the experimental measurements of Fig. 4(b), providing strong evidence that the anomalous scattering behavior arises from coherent thin-film interference rather than surface roughness or other geometric effects. These results demonstrate that even for a geometrically smooth metallic reflector, a lossy dielectric covering layer can substantially modify the angular scattering response through thickness- and frequency-dependent interference effects. Such phenomena have significant implications for terahertz channel modeling in indoor environments, where material-covered

metallic surfaces are commonly encountered and may exhibit strongly frequency-selective reflection characteristics that deviate markedly from simple Fresnel predictions.

B. Scattering by Covered Rough Surfaces

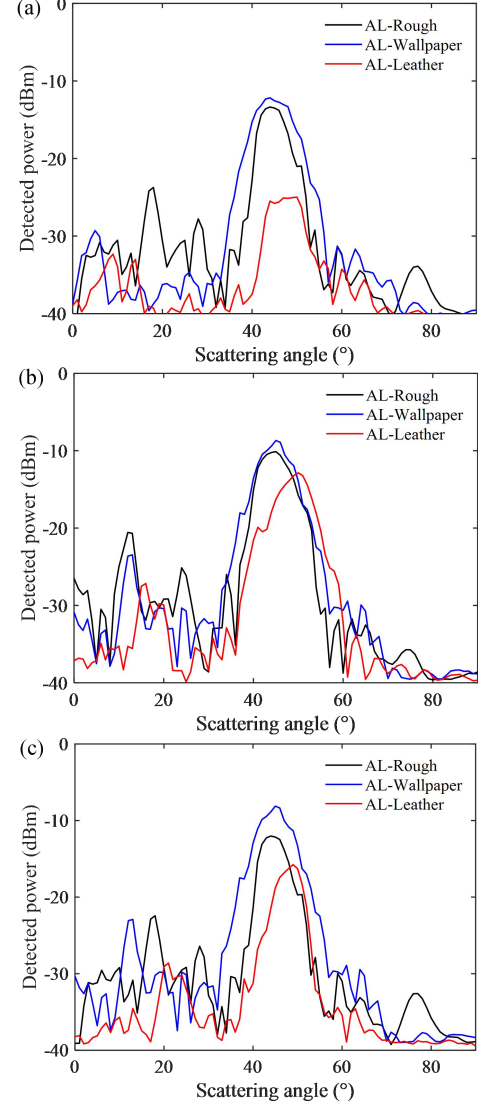


Fig. 5. Scattering distributions of a rough aluminum surface without and with material coverings: (a) 113 GHz; (b) 140 GHz; (c) 170 GHz.

Practical indoor environments frequently contain surfaces with non-negligible surface roughness arising from manufacturing processes, surface wear, or environmental degradation. To address this more general scenario, we further investigate the combined influence of material coverings and substrate surface roughness on THz channel scattering behavior. Specifically, wallpaper and leather samples were applied to an aluminum plate with controlled surface roughness, characterized by a root-mean-square (RMS) height of approximately 0.2 mm, as detailed in Fig. A1(f) in [52]. This roughness scale is comparable to the operating wavelength in the D-band frequency range, placing the surface in the intermediate roughness regime where both coherent (specular) and incoherent (diffuse) scattering components contribute significantly to the total reflected field [9, 14].

Measurements were performed at 113, 140, and 170 GHz under the same angular-scanning configuration described above.

As illustrated in Fig. 5, the scattering response of the material-covered rough aluminum surface exhibits distinct characteristics depending on the properties of the covering layer. For the wallpaper-covered configuration, a pronounced enhancement of the specular reflection component is observed across all three frequencies, accompanied by a notable suppression of off-specular scattering, particularly in the angular range of 10° - 30° . Compared with the bare rough aluminum surface, the resulting scattering profile becomes substantially more concentrated and approaches that of an idealized specular reflector. This behavior can be attributed to a redistribution of the angular scattering spectrum induced by the thin, low-loss dielectric layer. From an electromagnetic perspective, the dielectric covering modifies the effective boundary conditions at the air-substrate interface, resulting in an enhancement of the coherent reflection component and a corresponding suppression of diffuse scattering from the underlying rough metallic surface [53]. This phenomenon is analogous to the well-documented effect of dielectric coatings in reducing radar cross-section fluctuations from rough conducting surfaces, where the covering layer serves to partially smooth the effective electromagnetic interface [54, 55].

In contrast, the leather-covered configuration exhibits markedly different scattering characteristics. Although the leather covering partially suppresses the diffuse scattering induced by surface roughness, it simultaneously introduces pronounced power loss in the specular direction and an observable angular shift of the main lobe relative to the bare rough surface. This discrepancy between the wallpaper-covered and leather-covered responses arises primarily from the substantially different covering-layer thicknesses and the distinct mechanical compliance characteristics of both materials.

By jointly considering the reflection characteristics observed for single-material samples (Fig. 2), smooth covered surfaces (Fig. 4), and rough covered surfaces (Fig. 5), it can be found that the scattering response of a covered surface is no longer governed solely by the intrinsic reflectivity or permittivity of the covering material. Rather, the overall electromagnetic response is jointly determined by multiple interacting factors: the covering-layer thickness and its associated absorption characteristics, coherent multiple-reflection effects within the layer, the mechanical conformality between the covering and substrate, and the coupling between the dielectric layer properties and the substrate surface morphology. These underscore the importance of considering composite boundary conditions in terahertz channel modeling for realistic indoor environments, where material-covered surfaces with varying substrate roughness are commonly encountered.

IV. INDOOR ENVIRONMENT-AWARE SCATTERING

Unlike the controlled surface configurations examined previously, indoor scenarios introduce complex propagation effects jointly shaped by furniture arrangements, room geometry, wall and window compositions, and spatially structured reflection and scattering paths [5, 19, 56]. To characterize these environment-level phenomena, wide-angle bistatic measurements were conducted in a typical indoor conference-room setting.

Indoor channel measurements were conducted at two representative frequencies, 140 GHz and 220 GHz, for THz communications. In addition to the D-band experimental configuration described in Section II-B, an $\times 18$ frequency multiplier module (Ceyear 82406D) was employed together with corresponding horn antennas (Ceyear 89901S) and a calibrated power sensor (Ceyear 87106B), enabling terahertz signal generation and detection in the 220-325 GHz frequency band. For both frequency bands, a dielectric lens with a focal length of 35 cm was mounted in front of the horn antenna to collimate the radiated beam, thereby mitigating beam divergence and reducing free-space propagation loss over the extended indoor measurement distances. The measurements were performed in a conference room with dimensions of 7.69 m \times 6.93 m, representative of typical indoor meeting spaces encountered in office environments. As illustrated in Fig. 6, the transmitter (Tx) and receiver (Rx) were positioned on the east and west sides of the room, respectively, with a separation distance of 3.8 m. Both Tx and Rx were mounted on independent motorized rotary stages capable of full 360° azimuthal rotation, enabling comprehensive angular characterization of the indoor propagation channel. The antenna height was set to 1.15 m above the floor for both terminals, exceeding the height of window sills and major furniture items to minimize unintended blockage and ensure consistent line-of-sight conditions across angular configurations.

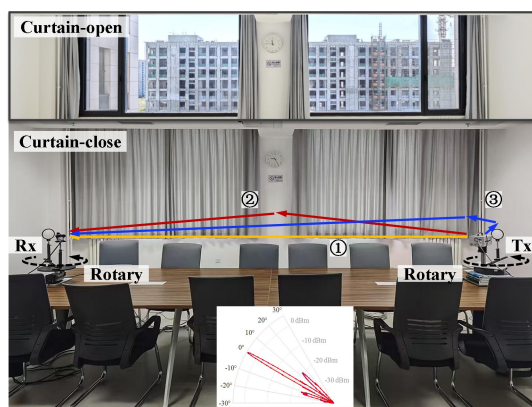


Fig. 6. Indoor terahertz channel measurement setup in a conference-room environment. Top inset: The conference room with window curtains fully opened (Curtain-open). Bottom inset: Effective radiation pattern of the antenna-lens setup at 140 GHz.

The room geometry and material composition are critical factors governing the indoor scattering environment. The south side of the room consists of glass windows and adjacent wall sections. A central wall segment with an east-west width

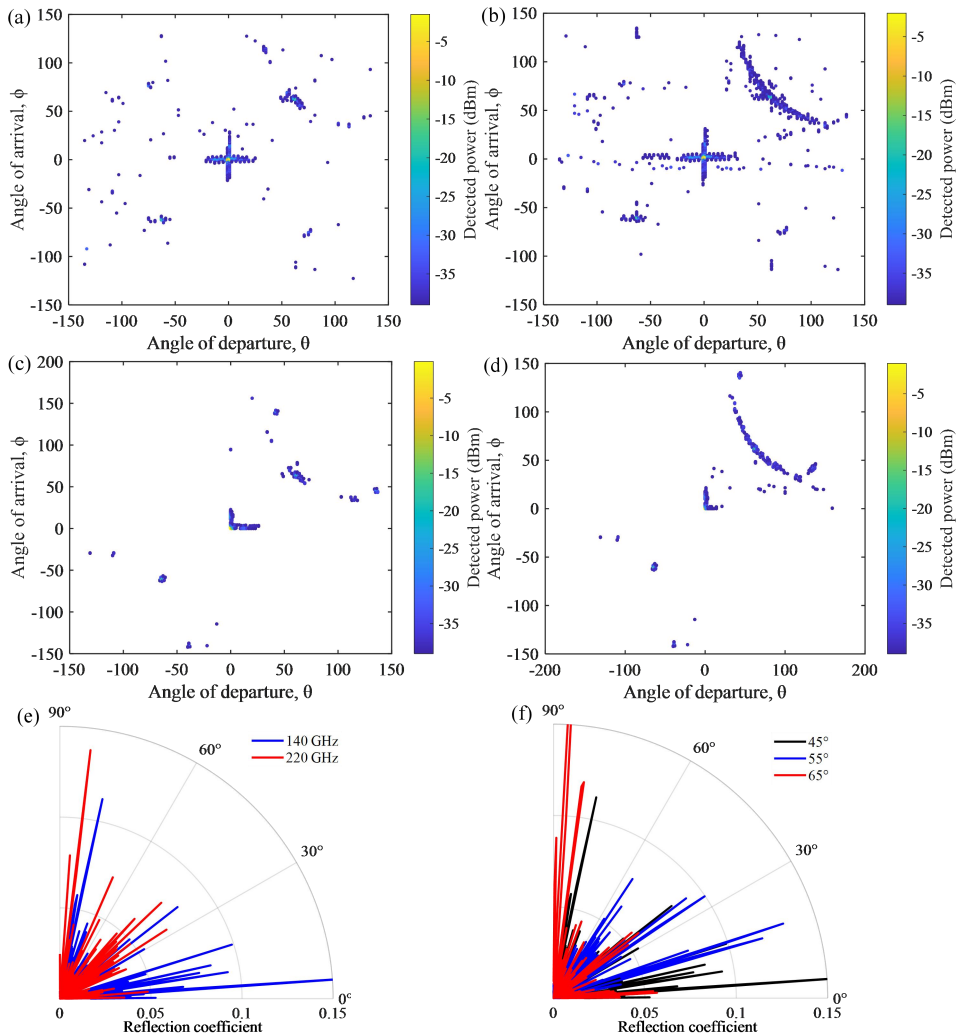


Fig. 7. (a) Measured scattering distribution at 140 GHz for the “Curtain-open” configuration. (b) Measured scattering distribution at 140 GHz for the “Curtain-close” configuration. (c) Measured scattering distribution at 220 GHz for the “Curtain-open” configuration. (d) Measured scattering distribution at 220 GHz for the “Curtain-close” configuration. (e) Calculated reflection coefficient at 140 GHz and 220 GHz for the “Curtain-close” configuration. (f) Calculated reflection coefficient as a function of incidence angle for the “Curtain-close” configuration at 140 GHz.

of approximately 0.4 m is positioned between two glass windows and serves as one of the dominant specular reflection surfaces. The glass windows on both sides have widths of 2.845 m and are equipped with fabric curtains that can be either opened or closed depending on the measurement scenario. The configuration illustrated in Fig. 6, labeled “Curtain-close,” corresponds to the scenario where the curtains fully cover the glass window surfaces, introducing folded-fabric scattering effects analyzed in Section IV and further supported in the Supplementary Information. On the north side of the room, two doorways (approximately 2.1 m wide each) are located near the corners, and a recessed bar counter (approximately 0.6 m deep and 3.53 m in east-west width) is situated at the center, forming another prominent specular-reflection region.

To achieve comprehensive angular characterization while maintaining practical measurement efficiency, the transmitter was operated with an angular step size of 2° . For each fixed Tx orientation, the receiver rotated continuously at an angular speed of $2^\circ/\text{s}$, while the received power was recorded at a sampling rate of 7 Hz. The scanning angular range for both Tx

and Rx was defined with respect to the line-of-sight direction and spanned $\pm 135^\circ$, covering a total azimuthal range of 270° . The positive angular direction corresponds to rotation toward the window (south) side of the room, whereas the negative direction corresponds to rotation toward the bar-counter (north) side. In total, 801,826 measurement samples were collected, with each sample consisting of the transmit steering angle θ , the receive observation angle ϕ , and the measured received power $P(\theta, \phi)$.

The bottom inset of Fig. 6 presents the effective radiation pattern of the antenna-lens assembly, which serves as a reference for interpreting the subsequent indoor scattering measurements. The transmitted beam exhibits strong directivity with a narrow main lobe, indicating a highly concentrated angular power distribution characteristic of terahertz systems. In addition to the main lobe, two sidelobes are observed at approximately $\pm 13^\circ$ from the boresight direction. These sidelobe components, although substantially weaker than the main beam, can illuminate reflecting surfaces at off-axis angles and thereby give rise to additional detectable propagation paths beyond the dominant specular direction.

Fig. 7(a) presents the full-angle scattering distribution measured at 140 GHz in the conference room with window curtains fully opened, corresponding to the “Curtain-open” configuration illustrated in the top inset of Fig. 6. When both $\theta > 0^\circ$ and $\varphi > 0^\circ$, corresponding to orientations toward the window-facing (south) side of the room, a dominant high-power scattering region is observed around 61° . Based on geometric analysis of the room layout, these components are attributed to specular reflections from the central wall segment (approximately 0.4 m in width) positioned between the two windows. Similarly, for $\theta < 0^\circ$ and $\varphi < 0^\circ$, another high-power scattering region appears around -61° , corresponding to reflections from the bar-counter wall on the north side. Notably, the south-side scattering region extends over a broader angular range compared to the north side, attributable to the combined effects of partially visible curtain edges, aluminum window frames, and local structural discontinuities that jointly enhance angular spreading in the window-facing region.

To examine how the introduction of a spatially structured element modifies indoor propagation characteristics - building upon the structure-induced scattering mechanisms established in Sections II-C and III - the curtains were deployed to fully cover the windows, corresponding to the “Curtain-close” configuration. The analysis focuses on the angular region where $\theta > 0^\circ$ and $\varphi > 0^\circ$. As shown in Fig. 7(b), in addition to the original specular-reflection region associated with the central wall segment, a dense set of additional detectable propagation components emerges, extending laterally toward the curtain-covered window areas and spanning approximately $\pm 35^\circ$ relative to the primary specular-reflection region. Importantly, the strength of the original specular reflection from the central wall segment remains largely unchanged, indicating that the curtain-induced scattering represents additional propagation paths rather than a redistribution of existing reflected energy. These additional components arise from the combination of the curtain’s intrinsic reflective properties (characterized in Fig. 2(b)) and its folded geometric structure, which together introduce diffuse scattering mechanisms consistent with the material-covered surface analysis in Section III.

In regions where $\theta \cdot \varphi < 0$ (i.e., transmitter and receiver oriented toward opposite sides of the room), detected signal components are generally weak and exhibit spatially irregular distributions. These components represent the ensemble of observable propagation contributions jointly shaped by material properties, environmental geometry, and measurement system characteristics, primarily originating from higher-order reflections, diffuse scattering, sidelobe-assisted propagation paths, and partially captured specular reflections due to finite receiver angular coverage.

To isolate frequency-dependent effects, additional measurements were performed at 220 GHz for both “Curtain-open” and “Curtain-close” configurations, with the angular scan restricted to the region where $\theta \cdot \varphi > 0$, as shown in Fig. 7(c) and Fig. 7(d). This region is dominated by specular components, making curtain-induced variations the

primary observable factor. As anticipated, curtain deployment significantly enhances the angular scattering response. Due to the increased directivity at 220 GHz, detectable components in the region where $\theta < 0^\circ$ and $\varphi < 0^\circ$ remain nearly unchanged in both spatial extent and power level. It should be noted that in the “Curtain-close” configuration, a portion of curtain-related scattered energy may not be fully captured due to finite angular coverage, implying that the measured scattering distributions represent conservative estimates of actual channel richness.

To provide physical interpretation of the curtain-induced angular scattering enhancement, a modeling framework combining local Fresnel reflection for layered media with physical-optics (PO) coherent integration is developed [57]. The model focuses on the “Curtain-close” configuration, where the folded curtain introduces a spatially structured surface that gives rise to additional scattering paths beyond those associated with the bare glass window. The framework is intended to capture the relative angular redistribution of reflected energy rather than absolute channel response. Consider a plane wave with frequency f and incident angle θ_i impinging on a curtain structure deployed in front of a glass window. The curtain surface profile is modeled as a one-dimensional (1D) cosinoidal (sinusoidal) function along the horizontal coordinate y :

$$z(y) = A_c \cos\left(\frac{2\pi y}{G_c}\right) \quad (11)$$

where A_c and G_c denote the amplitude and spatial period of the curtain folds, respectively. The local surface tilt angle is given by:

$$\alpha(y) = \tan^{-1}\left(\frac{dz}{dy}\right) \quad (12)$$

which determines the local incident angle $\theta_{loc}(y)$ between the incident wave vector and the local outward surface normal. The electromagnetic response of each illuminated surface element is represented by a local reflection weight. For the practical window configuration, the structure is modeled as a multilayer stack consisting of air, curtain fabric, air gap, glass, and air. The local reflection coefficient under vertical polarization (consistent with the experimental configuration) is expressed as:

$$\rho_v(y) = \frac{n_1 \cos(\theta_1) - n_2 \cos(\theta_2)}{n_1 \cos(\theta_1) + n_2 \cos(\theta_2)} \quad (13)$$

where n_1 and n_2 denote the refractive indices of air and the curtain layer, respectively. The parameter θ_1 represents the local incident angle $\theta_{loc}(y)$ in air, and θ_2 represents the corresponding transmission angle in the curtain layer, determined by Snell’s law $n_1 \sin \theta_1 = n_2 \sin \theta_2$. Although (13) is written in simplified Fresnel form for clarity, $\rho_v(y)$ is evaluated numerically via a coherent multilayer transfer-matrix formulation that accounts for multiple internal reflections and phase accumulations within the layered structure [58].

The angular scattering response is obtained using a physical-optics formulation, wherein the scattered field toward observation angle θ_s is calculated by coherently integrating

contributions from all illuminated surface elements over the effective aperture:

$$R_v(\theta_s) = \frac{\left| \int_{-L/2}^{L/2} \rho_v(y) A(y) \exp(i\Delta\Phi(y)) dy \right|^2}{|E_{ref}|^2} \quad (14)$$

where $\Delta\Phi(y)$ accounts for the geometry-induced optical path difference and $A(y)$ accounts for the Jacobian between the parameter coordinate y and the surface arc length ds . In 1D, $ds = \sqrt{\sec(\alpha(y))} dy$, so we set $A(y) = \sqrt{\sec(\alpha(y))}$ when integrating field contributions over the surface. The reference field E_{ref} corresponds to the specular reflected field from a planar reference configuration ($A_c = 0$) with identical multilayer composition and illuminated aperture, such that normalization emphasizes the curtain-induced angular redistribution.

Fig. 7(e) presents the calculated angular scattering distributions at 140 GHz and 220 GHz for a curtain-air-window structure using a cosine ripple as a first-order geometric proxy for folds, with ripple amplitude $A_c = 5$ cm and spatial period $G_c = 25$ cm. The model predicts strong angular redistribution over a wide range because the local surface-normal variations are large compared with the wavelength. In practice, real curtains exhibit fold-to-fold variability and multi-scale perturbations, which further smear out any discrete periodic features; this explains why the measured distributions do not show stable grating orders [57]. This model prediction is validated by the experimental observations in Fig. 7(b) and Fig. 7(d), where similarly broad angular spreading without pronounced periodic features is consistently observed for the ‘‘Curtain-close’’ configuration.

To further substantiate the structure-induced scattering mechanism, controlled experiments with specific curtain-fold configurations were conducted. As detailed in Fig. S2 of the Supplementary Information, scattering measurements at 113, 140, and 170 GHz were compared against those obtained for a flat curtain under identical angular configurations. At each frequency, transitioning from flat to folded curtain configuration significantly suppresses the specular reflection component at 45° (corresponding to the incidence angle), while generating additional scattering detectable over a broad angular range without stable periodic features. These results corroborate the model predictions. Meanwhile, detected power at 135° (corresponding to the LoS transmission direction) remains consistently high, indicating that the folded structure primarily redistributes reflected power over a wide angular range rather than attenuating overall transmission.

Since incidence angle varies continuously during full-angle indoor scans, additional calculations examining different incidence angles are presented in Fig. 7(f). Although detailed angular distributions depend on incidence angle, a common characteristic emerges: non-negligible scattered energy remains observable across a wide angular range for all configurations examined. These findings suggest that material- and structure-induced scattering mechanisms offer a potentially low-cost approach for shaping indoor terahertz propagation, with practical benefits for coverage enhancement

and link robustness in future indoor communication systems [59,60].

V. CONCLUSION

As wireless communication systems progressively extend into THz frequency bands, understanding the intricate interactions between THz channels and realistic environments becomes increasingly critical for system design and deployment. This work has systematically investigated structure-induced surface scattering phenomena at THz frequencies through coordinated experimental measurements and theoretical modeling. The dielectric characterization of six common indoor surfaces revealed substantial variations in electromagnetic properties, with the pine wood sample exhibiting particularly notable structural inhomogeneity arising from its periodic earlywood-latewood arrangement. A beam-propagation modeling (BPM) framework was developed to quantitatively link this internal periodic structure to the observed angular scattering characteristics, demonstrating that the dominant angular features are primarily governed by the effective period, tilt angle, and duty cycle of the growth-layer structure.

For material-covered surface configurations, the investigation revealed that thin dielectric covering layers can fundamentally alter the electromagnetic response through coherent thin-film interference effects, with the leather-covered aluminum surface exhibiting pronounced frequency-dependent reflection suppression near 170 GHz. Furthermore, the wallpaper-covered rough surface measurements demonstrated that low-loss dielectric coatings can redistribute the angular scattering spectrum, enhancing specular reflection while suppressing diffuse components from the underlying rough substrate. Wide-angle indoor measurements in a conference-room environment demonstrated that structured elements such as folded curtains can generate additional channel paths spanning approximately $\pm 35^\circ$ relative to the specular direction, significantly enhancing spatial coverage. These findings collectively establish that surface material properties, structural configurations, and environmental geometry jointly govern THz channel characteristics, and that leveraging intrinsic scattering properties of existing surfaces offers a practical pathway for robust non-line-of-sight link construction.

REFERENCES

- [1] W. M. Othman et al., ‘‘Key enabling technologies for 6G: The role of UAVs, terahertz communication, and intelligent reconfigurable surfaces in shaping the future of wireless networks,’’ *J. Sens. Actuator Netw.*, vol. 14, no. 2, p. 30, 2025.
- [2] J. Ma et al., ‘‘Terahertz Channels in Atmospheric Conditions: Propagation Characteristics and Security Performance,’’ *Fundam. Res.*, vol. 5, no. 2, pp. 526-555, 2025.
- [3] J. Ma, P. Li, and W. Liu, *Terahertz Channel Measurement, Modeling, and Security Properties: Fundamentals, Techniques, and Applications*. Boca Raton, FL, USA: CRC Press, 2025.
- [4] J. Ma, R. Shrestha, L. Moeller, and D. M. Mittleman, ‘‘Invited Article: Channel performance for indoor and outdoor terahertz wireless links,’’ *APL Photon.*, vol. 3, no. 5, p. 051601, 2018, doi: 10.1063/1.5014037.

- [5] F. Taleb, G. G. Hernandez-Cardoso, E. Castro-Camus, and M. Koch, "Transmission, Reflection, and Scattering Characterization of Building Materials for Indoor THz Communications," *IEEE Trans. THz Sci. Technol.*, vol. 13, no. 5, pp. 421-430, 2023, doi: 10.1109/THZ.2023.3281773.
- [6] T. S. Rappaport, R. W. Heath Jr., R. C. Daniels, and J. N. Murdock, *Millimeter Wave Wireless Communications*. Upper Saddle River, NJ, USA: Pearson Education, 2014.
- [7] Y. Monnai, X. Lu, and K. Sengupta, "Terahertz beam steering: from fundamentals to applications," *J. Infrared Millim. Terahertz Waves*, vol. 44, no. 3, pp. 169-211, 2023.
- [8] Y. Karacora, A. Umra, and A. Sezgin, "Robust Communication Design in RIS-Assisted THz Channels," *IEEE Open J. Commun. Soc.*, vol. 6, pp. 3029-3043, 2025, doi: 10.1109/OJCOMS.2025.3541315.
- [9] P. Li et al., "Scattering and Eavesdropping in Terahertz Wireless Link by Wavy Surfaces," *IEEE Trans. Antennas Propag.*, vol. 71, no. 4, pp. 3590-3597, 2023, doi: 10.1109/TAP.2023.3241333.
- [10] J. M. Seifert, G. G. Hernandez-Cardoso, M. Koch, and E. Castro-Camus, "Terahertz beam steering using active diffraction grating fabricated by 3D printing," *Opt. Express*, vol. 28, no. 15, pp. 21737-21744, 2020.
- [11] Z. Wang et al., "Fast-printed, large-area and low-cost terahertz metasurface using laser-induced graphene," *Carbon*, vol. 187, pp. 256-265, 2022.
- [12] C. Han et al., "Terahertz wireless channels: A holistic survey on measurement, modeling, and analysis," *IEEE Commun. Surv. Tutor.*, vol. 24, no. 3, pp. 1670-1707, 2022.
- [13] S. Ju et al., "Scattering mechanisms and modeling for terahertz wireless communications," in *Proc. IEEE Int. Conf. Commun. (ICC)*, Shanghai, China, 2019, pp. 1-7.
- [14] J. Ma, R. Shrestha, W. Zhang, L. Moeller, and D. M. Mittleman, "Terahertz Wireless Links using Diffuse Scattering from Rough Surfaces," *IEEE Trans. Terahertz Sci. Technol.*, vol. 9, no. 5, p. 460, 2019, doi: 10.1109/tthz.2019.2933166.
- [15] Y. Wang et al., "Measured reflection and transmission properties of building materials for indoor THz communication," *IEEE Antennas Wireless Propag. Lett.*, vol. 22, no. 6, pp. 1361-1365, 2023.
- [16] Z. Chang et al., "Frequency-angle two-dimensional reflection coefficient modeling based on terahertz channel measurement," *Front. Inf. Technol. Electron. Eng.*, vol. 24, no. 4, pp. 626-632, 2023.
- [17] T. S. Rappaport, K. A. Remley, C. Gentile, A. F. Molisch, and A. Zajić, *Radio Propagation Measurements and Channel Modeling*. Cambridge University Press, 2022.
- [18] D. Li et al., "Experimental and theoretical exploration of terahertz channel performance through glass doors," *Nano Commun. Netw.*, vol. 39, p. 100496, 2024.
- [19] M. Zhai et al., "Broadband transmission characterization of indoor building materials using terahertz time-domain spectroscopy," *J. Opt. Soc. Am. B*, vol. 42, no. 2, pp. 201-205, 2025.
- [20] M. Urahashi and A. Hirata, "Complex permittivity evaluation of building materials at 200-500 GHz using THz-TDS," in *Proc. Int. Symp. Antennas Propag. (ISAP)*, Osaka, Japan, 2020, pp. 539-540.
- [21] B. Xue, K. Haneda, C. Icheln, J. Ala-Laurinaho, and J. Tuomela, "Complex permittivity characterization of low-loss dielectric slabs at sub-THz," *IEEE Access*, vol. 12, pp. 150693-150701, 2024, doi: 10.1109/ACCESS.2024.3479908.
- [22] D. Shakya, S. Ju, O. Kanhere, H. Poddar, Y. Xing, and T. S. Rappaport, "Radio propagation measurements and statistical channel models for outdoor urban microcells in open squares and streets at 142, 73, and 28 GHz," *IEEE Trans. Antennas Propag.*, vol. 72, no. 4, pp. 3580-3595, 2024.
- [23] J. Cui et al., "Terahertz channel modeling based on surface sensing characteristics," *Nano Commun. Netw.*, vol. 42, p. 100533, 2024.
- [24] A. A. Firoozi and A. A. Firoozi, "A comprehensive survey: The role of terahertz communication systems in urban infrastructure development," *Measurement*, vol. 251, p. 117318, 2025, doi: 10.1016/j.measurement.2025.117318.
- [25] N. A. Abbasi et al., "THz band channel measurements and statistical modeling for urban D2D environments," *IEEE Trans. Wireless Commun.*, vol. 22, no. 3, pp. 1466-1479, 2022.
- [26] A. Li et al., "Study on non-destructive detection technology of water content and defects in construction materials based on transmission terahertz system," *J. Build. Eng.*, vol. 104, p. 112452, 2025.
- [27] Y. Xu and X. Jiang, "Nondestructive testing and imaging of corrosion thickness of steel plates using THz-TDS," *Infrared Phys. Technol.*, vol. 127, p. 104467, 2022.
- [28] V. Mikhnev, D. But, T. Zugno, M. Boban, J. Eichinger, and W. Knap, "Measurement and Modelling of Dielectric Properties of Building Materials at Sub-THz Frequencies," in *Proc. Eur. Conf. Antennas Propag. (EuCAP)*, Stockholm, Sweden, 2025, pp. 1-5.
- [29] Y. Wang, Y. Liu, X. Liao, Z. Yu, G. Wang, and J. Zhang, "Complex permittivity extraction of building materials from transmission/reflection measurements at Sub-THz band," in *Proc. IEEE Globecom Workshops (GC Wkshps)*, Kuala Lumpur, Malaysia, 2023, pp. 1934-1939.
- [30] C. Binggeli, *Materials for interior environments*. Hoboken, NJ, USA: John Wiley & Sons, 2008.
- [31] F. Sheikh et al., "Scattering and Roughness Analysis of Indoor Materials at Frequencies from 750 GHz to 1.1 THz," *IEEE Trans. Antennas Propag.*, vol. 69, no. 11, pp. 7820-7829, 2021, doi: 10.1109/TAP.2021.3076577.
- [32] T. Inagaki, B. Ahmed, I. D. Hartley, S. Tsuchikawa, and M. Reid, "Simultaneous prediction of density and moisture content of wood by terahertz time domain spectroscopy," *J. Infrared Millim. Terahertz Waves*, vol. 35, no. 11, pp. 949-961, 2014, doi: 10.1007/s10762-014-0095-7.
- [33] M. Koch, S. Hunsche, P. Schumacher, M. C. Nuss, J. Feldmann, and J. Fromm, "THz-imaging: a new method for density mapping of wood," *Wood Sci. Technol.*, vol. 32, no. 6, pp. 421-427, 1998.
- [34] T. D. Dorney, R. G. Baraniuk, and D. M. Mittleman, "Material parameter estimation with terahertz time-domain spectroscopy," *J. Opt. Soc. Am. A*, vol. 18, no. 7, pp. 1562-1571, 2001.
- [35] R. Zhao, Q. Niu, G. Murtaza, G. Zhang, and Y. Yang, "Integrated identification and detection of hydration state and its evolution using terahertz technology," *Talanta*, vol. 281, p. 126943, 2025.
- [36] Q. Niu et al., "Ultra-Broadband, Rapid, and Trace Terahertz Fingerprint Detection via Resonance Interaction Enhancement with an Unpatterned Dielectric Wafer," *Laser Photon. Rev.*, vol. 20, no. 3, Art. no. e202500848, 2026, doi: 10.1002/lpor.202500848.
- [37] J. Björklund et al., "Cell size and wall dimensions drive distinct variability of earlywood and latewood density in Northern Hemisphere conifers," *New Phytol.*, vol. 216, no. 3, pp. 728-740, 2017.
- [38] M. Kashima, S. Tsuchikawa, and T. Inagaki, "Simultaneous detection of density, moisture content and fiber direction of wood by THz time-domain spectroscopy," *J. Wood Sci.* vol. 66, no. 1, p. 27, 2020.
- [39] G. I. Torgovnikov, "Dielectric properties of wood-based materials," in *Dielectric Properties of Wood and Wood-Based Materials*, Berlin, Germany: Springer-Verlag, 1993, pp. 135-159.
- [40] D. Yevick and L. Thylen, "Analysis of gratings by the beam-propagation method," *J. Opt. Soc. Am.*, vol. 72, no. 8, pp. 1084-1089, 1982.
- [41] L. Thylen, "The beam propagation method: an analysis of its applicability," *Opt. Quantum Electron.*, vol. 15, no. 5, pp. 433-439, 1983.
- [42] M. Feit and J. Fleck Jr., "Light propagation in graded-index optical fibers," *Appl. Opt.*, vol. 17, no. 24, pp. 3990-3998, 1978.
- [43] J. Van Roey, J. Van der Donk, and P. Lagasse, "Beam-propagation method: analysis and assessment," *J. Opt. Soc. Am.*, vol. 71, no. 7, pp. 803-810, 1981.
- [44] H. Kogelnik, "Coupled wave theory for thick hologram gratings," *Bell Syst. Tech. J.*, vol. 48, no. 9, pp. 2909-2947, 1969.
- [45] D. Banerjee, W. v. Spiegel, M. D. Thomson, S. Schabel, and H. G. Roskos, "Diagnosing water content in paper by terahertz radiation," *Opt. Express*, vol. 16, no. 12, pp. 9060-9066, 2008, doi: 10.1364/OE.16.009060.
- [46] N. Stathopoulos et al., "Reflection and transmission calculations in a multilayer structure with coherent, incoherent, and partially coherent interference, using the transmission line method," *Appl. Opt.*, vol. 54, no. 6, pp. 1492-1504, 2015.
- [47] F. Abeles, "Optical properties of thin absorbing films," *J. Opt. Soc. Am.*, vol. 47, no. 6, pp. 473-482, 1957.
- [48] A. Sarangan, *Optical thin film design*. Boca Raton, FL, USA: CRC Press, 2020.
- [49] S. Perea-Puente and F. J. Rodríguez-Fortuño, "Complex refraction metasurfaces for locally enhanced propagation through opaque media," *Laser Photon. Rev.*, vol. 18, no. 5, p. 2300867, 2024.
- [50] K. Ohta and H. Ishida, "Matrix formalism for calculation of electric field intensity of light in stratified multilayered films," *Appl. Opt.*, vol. 29, no. 13, pp. 1952-1959, 1990.
- [51] O. S. Heavens, *Optical properties of thin solid films*. New York, NY, USA: Dover Publications, 1991.
- [52] J. Liu et al., "High-speed surface property recognition with a 140 GHz frequency," *Appl. Sci.*, vol. 14, no. 10, p. 4321, 2024.

- [53] T. Nordam, P. A. Letnes, I. Simonsen, and A. A. Maradudin, "Satellite peaks in the scattering of light from the two-dimensional randomly rough surface of a dielectric film on a planar metal surface," *Opt. Express*, vol. 20, no. 10, pp. 11336-11350, 2012.
- [54] R. Azadegan and K. Sarabandi, "Analytical formulation of the scattering by a slightly rough dielectric boundary, covered with a homogenous dielectric layer," in *Proc. IEEE Antennas Propag. Soc. Int. Symp. (APS/URSI)*, Columbus, OH, USA, 2003, vol. 3, pp. 420-423.
- [55] P. Imperatore, A. Iodice, and D. Riccio, "Electromagnetic wave scattering from layered structures with an arbitrary number of rough interfaces," *IEEE Trans. Geosci. Remote Sens.*, vol. 47, no. 4, pp. 1056-1072, 2009.
- [56] M. Wang et al., "Reflection characteristics measurements of indoor wireless link in D-band," *Sensors*, vol. 22, no. 18, p. 6908, 2022.
- [57] I. Simonsen, "Optics of surface disordered systems: a random walk through rough surface scattering phenomena," *IEEE Trans. Geosci. Remote Sens.*, vol. 181, no. 1, pp. 1-103, 2010.
- [58] C. C. Katsidis and D. I. Siapkas, "General transfer-matrix method for optical multilayer systems with coherent, partially coherent, and incoherent interference," *Appl. Opt.*, vol. 41, no. 19, pp. 3978-3987, 2002.
- [59] V. Petrov, A. Pyattaev, D. Moltchanov, and Y. Koucheryavy, "Terahertz band communications: Applications, research challenges, and standardization activities," in *Proc. Int. Congr. Ultra Modern Telecommun. Control Syst. Workshops (ICUMT)*, Lisbon, Portugal, 2016, pp. 183-190.
- [60] S. Sharma, P. K. Singya, K. Deka, C. Adjih, and M. Sharma, "Terahertz communication: State-of-the-art and future directions," *IEEE Open J. Commun. Soc.*, vol. 6, pp. 6281-6322, 2025, doi: 10.1109/OJCOMS.2025.3592365.